MUSE sneaks a peek at extreme ram-pressure stripping events. I. A kinematic study of the archetypal galaxy ESO137−001.*

Michele Fumagalli[1,2]†, Matteo Fossati[3,4], George K.T. Hau[5], Giuseppe Gavazzi[6],
Richard Bower[1], Ming Sun[7], Alessandro Boselli[8]

[1]*Institute for Computational Cosmology, Department of Physics, Durham University, South Road, Durham, DH1 3LE, UK*
[2]*Carnegie Observatories, 813 Santa Barbara Street, Pasadena, CA 91101, USA*
[3]*Universitäts-Sternwarte München, Scheinerstrasse 1, D-81679 München, Germany*
[4]*Max-Planck-Institut für Extraterrestrische Physik, Giessenbachstrasse, D-85748 Garching, Germany*
[5]*European Southern Observatory, Alonso de Cordova 3107, Santiago, Chile*
[6]*Università di Milano-Bicoocca, Piazza della scienza 3, Milano, Italy*
[7]*Department of Physics, University of Alabama in Huntsville, Huntsville, AL 35899, USA*
[8]*Laboratoire d'Astrophysique de Marseille - LAM, Université d'Aix-Marseille & CNRS, UMR7326, 38 rue F. Joliot-Curie, F-13388 Marseille Cedex 13, France*

ABSTRACT

We present MUSE observations of ESO137−001, a spiral galaxy infalling towards the center of the massive Norma cluster at $z \sim 0.0162$. During the high-velocity encounter of ESO137−001 with the intracluster medium, a dramatic ram-pressure stripping event gives rise to an extended gaseous tail, traced by our MUSE observations to > 30 kpc from the galaxy center. By studying the Hα surface brightness and kinematics in tandem with the stellar velocity field, we conclude that ram pressure has completely removed the interstellar medium from the outer disk, while the primary tail is still fed by gas from the galaxy center. Gravitational interactions do not appear to be a primary mechanism for gas removal. The stripped gas retains the imprint of the disk rotational velocity to ~ 20 kpc downstream, offering evidence that ESO137−001 is fast moving along a radial orbit in the plane of the sky. Beyond ~ 20 kpc, a greater degree of turbulence is seen, with velocity dispersion up to $\gtrsim 100$ km s^{-1}. For a model-dependent infall velocity of $v_{\rm inf} \sim 3000$ km s^{-1}, we conclude that the transition from laminar to turbulent flow in the tail occurs on timescales of ~ 6.5 Myr. Our work demonstrates the terrific potential of MUSE for detailed studies of how ram-pressure stripping operates on small scales, providing a deep understanding of how galaxies interact with the dense plasma of the cluster environment.

Key words: hydrodynamics – turbulence – techniques: spectroscopic – galaxies: ISM – galaxies: clusters: individual: ESO137-001 – galaxies: kinematics and dynamics

1 INTRODUCTION

The discovery of a well-defined color bimodality in galaxy populations at redshifts $z = 0 - 2$ is arguably one of the most significant legacy of galaxy surveys (e.g. Bower et al. 1992; Strateva et al. 2001; Baldry et al. 2004; Bell et al. 2004; Weiner et al. 2005; Brammer et al. 2009). A major task for modern studies of galaxy formation is therefore to understand how and when internal processes and environment drive the evolution of galaxies from the blue to the red cloud. While internal mechanisms, including ejective feedback from supernovae or active galactic nuclei, are deemed responsible for suppressing and quenching star formation at all densities, envi-

ronmental processes in the form of tidal interactions, harassment, and ram-pressure or viscous stripping are key players in shaping the observed color bimodality within rich galaxy clusters, especially at the faint end of the galaxy luminosity function (e.g. Larson et al. 1980; Hashimoto et al. 1998; Lewis et al. 2002; Gavazzi et al. 2002; Kauffmann et al. 2004; Balogh et al. 2004; Boselli & Gavazzi 2006; Boselli et al. 2008; Gavazzi et al. 2010; Smith et al. 2012a; Dressler et al. 2013).

The smoking gun of ongoing environmental transformation in nearby clusters is the disturbed gas morphology seen in "head-tail" radio continuum emission or in prominent Hα tails arising from galaxies moving towards the centers of massive clusters, as visible in Coma, Virgo, and A1367 (e.g. Gavazzi & Jaffe 1985; Gavazzi et al. 2001; Yoshida et al. 2002; Cortese et al. 2006; Kenney et al. 2008; Yagi et al. 2010; Fossati et al. 2012). Detailed multi-wavelength studies of these archetypal galaxies which are under-
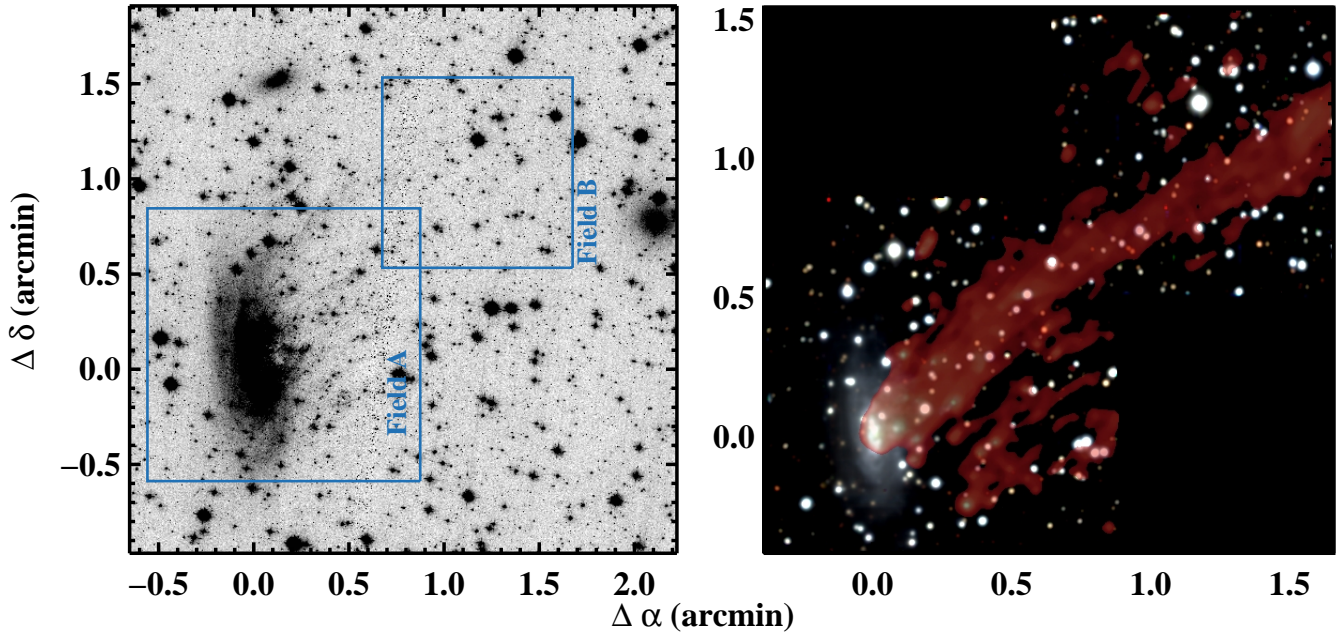
Figure 1. *Left:* Archival HST/ACS image in the F475W filter (PID 11683; PI Ming Sun) with, superposed, the MUSE field of view at the two locations targeted by our observations. In this figure, north is up and east is to the left. The coordinate system is centered at the J2000 position of ESO137−001 (α =16:13:27.3, δ =-60:45:51). At the redshift of ESO137−001, $1' = 18.4$ kpc. *Right:* RGB color image obtained combining images extracted from the MUSE datacube in three wavelength intervals ($\lambda = 5000 - 6000$ Å for the B channel, $\lambda = 6000 - 7000$ Å for the G channel, and $\lambda = 7000 - 8000$ Å for the R channel). A map of the Hα flux is overlaid in red using a logarithmic scale, revealing the extended gas tail that originates from the high-velocity encounter of ESO137−001 with the intracluster medium.

going extreme gravitational and hydrodynamic transformations in the harsh cluster environment (e.g. Vollmer et al. 2004; Sun et al. 2006; Fumagalli & Gavazzi 2008; Hester et al. 2010; Fumagalli et al. 2011; Arrigoni Battaia et al. 2012; Fossati et al. 2012; Kenney et al. 2014; Ebeling et al. 2014) become an invaluable tool for unveiling the rich physics responsible for the morphological and color transformation of cluster galaxies. In synergy with models and numerical simulations (e.g. Gunn & Gott 1972; Nulsen 1982; Moore et al. 1996; Quilis et al. 2000; Vollmer et al. 2001a; Bekki & Couch 2003; Kronberger et al. 2008; Tonnesen & Bryan 2010; Ruszkowski et al. 2014), these peculiar systems are in fact ideal laboratories to constrain the efficiency with which gas can be removed, quenching star formation. Extrapolated to the more general cluster population, results from these studies offer a unique perspective for how the red sequence is assembled in dense environments.

A particularly stunning example of a galaxy which is undergoing environmental transformation is ESO137−001, member of the massive Norma cluster. The Norma cluster, also known as A3627, has a dynamical mass of $M_{\mathrm{dyn,cl}} \sim 1 \times 10^{15}$ M$_\odot$ and lies in the Great Attractor region at a radial velocity of $v_{\mathrm{cl}} = 4871 \pm 54$ km s^{-1}, or redshift $z_{\mathrm{cl}} = 0.01625 \pm 0.00018$ (Woudt et al. 2008; Nishino et al. 2012). ESO137−001 is located at a projected distance of only $14.5'$ from the central cluster galaxy WKK6269, corresponding to ~ 267 kpc for the adopted cosmology ($H_0 = 69.7$ and $\Omega_{\mathrm{m}} = 0.236$ for which $1' = 18.4$ kpc; Hinshaw et al. 2013). Observations across the entire electromagnetic spectrum, including X-ray, optical, infrared, and millimetric data (Sun et al. 2006, 2007, 2010; Sivanandam et al. 2010; Jachym et al. 2014), show that ESO137−001 is suffering from an extreme ram-pressure stripping event during its first approach to the center of A3627. Most notably, ESO137−001 exhibits a double tail which

extend for ~ 70 kpc as seen in X-ray, pointing in the opposite direction from the cluster center (Sun et al. 2006, 2010). This tail, which is also detected in Hα (Sun et al. 2007) and contains both cold and warm molecular gas (Sivanandam et al. 2010; Jachym et al. 2014), is thought to originate from the interaction between the hot intracluster medium (ICM) and the warm/cold insterstellar medium (ISM) which is being ablated from the stellar disk by ram pressure (e.g. Sun et al. 2010; Jachym et al. 2014).

A complete picture of how ram-pressure operates in this galaxy and how the cold, warm, and hot gas phases coexist and interact inside the extended tail requires a detailed knowledge of the gas kinematics and of emission-line ratios. To date, these diagnostics have been limited to pointed radio observations (Jachym et al. 2014) or spectroscopy of selected HII regions (Sun et al. 2007, 2010). To drastically improve the status of current observations, we exploit the unprecedented capabilities the Multi Unit Spectroscopic Explorer (MUSE; Bacon et al. 2010) at the UT4 Very Large Telescope. With its unique combination of high efficiency (~ 0.35 at 6800 Å), extended wavelength coverage ($\sim 4800 - 9300$ Å sampled at 1.25 Å), and large field of view ($1' \times 1'$ in Wide Field Mode, sampled with $0.2''$ pixels), MUSE is a unique instrument to map at optical wavelengths the kinematics and line ratios of the disk and tail of ESO137−001. In this paper, we present MUSE observations of ESO137−001 which were conducted as part of the science verification run. After discussing the data reduction (Sect. 2) and the data analysis technique (Sect. 3), we present a study of the kinematics of the Hα emitting gas and of the stellar disk of ESO137−001 (Sect. 4). Subsequent papers in this series (Fossati et al., in prep.) will analyze emission and absorption line ratios to characterize the physical properties of the emitting gas and of the stellar populations in the disk and tail of ESO137−001.

2 OBSERVATIONS AND DATA REDUCTION

ESO137−001 was observed with MUSE during the science veri-fication run on UT June 21, 2014, under program 60.A-9349(A) (PI Fumagalli, Hau, Slezak). Observations were conducted while the galaxy was transiting at airmass ~ 1.25, in photometric condi-tions and good seeing ($\sim 0.8'' - 0.7''$). The disk and the inner tail of ESO137−001 ("Field A" in Figure 1) were observed with three exposures of 900s each, with dithers of $13'' - 16''$ and a rotation of 90 degrees in the instrument position angle at each position. A single 900s exposure ("Field B" in Figure 1) was then acquired to cover the extent of the primary tail. Natural seeing mode and slow guiding mode were used.

The final data product is obtained using a combination of recipes from the early-release MUSE pipeline (v0.18.1) and a set of in-house IDL codes, which we have developed to improve the quality of the illumination, sky subtraction, and flux calibration of the MUSE data. First, using the MUSE pipeline, we construct for each IFU a master bias, a master flat field, and a master sky flat, together with a wavelength solution. Next, we apply these calibra-tions to each science exposure and to exposures of the standard star GD153, which was observed for 30s at the beginning of the night in photometric conditions. After computing the instrument response curve for flux calibration and the telluric correction spec-trum within the MUSE pipeline, we apply a smoothing kernel of 80 pixel to the obtained sensitivity function so as to remove resid-ual small-scale fluctuations in the instrument response, which are present in the current version of the MUSE pipeline. The quality of photometric calibration is confirmed by aperture photometry on the r-band image reconstructed from the final datacube, which is in ex-cellent agreement with r-band magnitudes in APASS, the AAVSO All-Sky Photometric Survey (Henden et al. 2012).

Using the MUSE pipeline, we then produce resampled dat-acubes for each exposure (in spaxels of 1.25Å and $0.2'' \times 0.2''$), also saving individual calibrated pixel tables which contain the data and variance pixels before interpolation. Cosmic rays are also iden-tified as 7σ outliers. At this stage, the MUSE pipeline could be used to compute the sky subtraction with the algorithm offered by the pipeline recipes. However, when sky subtraction is enabled, the re-constructed cube exhibits an evident variation in the illumination of each slice which, as noted in the pipeline manual, is currently not fully corrected by sky flats. Due to this variation, and perhaps to the particularly crowded nature of our field, the sky-subtracted cubes exhibit large negative residuals which would affect our subsequent analysis. To improve the data quality, we perform both an illumi-nation correction and sky subtraction, using a set of IDL proce-dures which we have specifically developed to handle the reduced MUSE pixel tables. First, the illumination correction is computed by fitting eight bright sky lines in all slices within each exposure and by normalizing them to the median flux distribution across the entire field of view. After applying this illumination correction, we then generate a sky model in each exposure by combining pixels of comparable wavelength and within the 20-30th flux percentiles in a master sky spectrum. This operation is performed on the pixel table, to improve the spectral sampling of the sky model. We then subtract the sky model from each pixel, by interpolating the master sky spectrum with a spline function. Following these procedures, we find that the newly reconstructed datacubes present a more uni-form illumination pattern and do not have evident residuals in the background level. As a further test of our procedure, we verify that the line flux from extragalactic sources in the sky-subtracted cubes and the non-sky subtracted cubes agree to within $\sim 2\%$. At each step, our IDL procedures propagate errors in the datacube which contains the pixel variance (also known as "stat" datacube).

At the end of the reduction, we combine the four exposures and we reconstruct the final datacube inside the MUSE pipeline, after having registered the astrometry to the available HST imaging with in-house IDL codes to achieve a sub-arcsecond precision in both the absolute and relative astrometry. Data are interpolated over a regular grid of $0.2''$ spatially and 1.25Å spectrally. Finally, we apply the heliocentric correction to the wavelengths computed in air by the pipeline. An RGB color image produced by combining three slices of 1000Å from the final MUSE datacube is shown in Figure 1. In this figure, we also superimposed a map of the Hα flux, obtained as described in the next section.

The final datacube has an excellent image quality, with full width at half maximum (FWHM) of $0.73'' \pm 0.05''$ for point sources in the field. We also characterize the noise properties by measuring in each spatial pixel the standard deviation of fluxes in the wavelength interval $6740 - 6810$Å, which is clean of bright sky line residuals. The mean surface brightness limit at 3σ confi-dence level is 3.0×10^{-18} erg s^{-1} cm^{-2} Å^{-1} arcsec^{-2} for Field A and 4.9×10^{-18} erg s^{-1} cm^{-2} Å^{-1} arcsec^{-2} for Field B. Noise properties are uniform across the field, with a spatial vari-ation expressed in unit of standard deviation about the mean of 4×10^{-19} erg s^{-1} cm^{-2} Å^{-1} arcsec^{-2} for Field A and 1×10^{-18} erg s^{-1} cm^{-2} Å^{-1} arcsec^{-2} for Field B. For an unresolved line of $\Delta\lambda = 2.55$Å at ~ 6700Å, the line surface brightness limit becomes 7.6×10^{-18} erg s^{-1} cm^{-2} arcsec^{-2} for Field A and 1.2×10^{-17} erg s^{-1} cm^{-2} arcsec^{-2} for Field B.

3 EMISSION AND ABSORPTION LINE MODELING

To characterize the kinematics of the gas in the disk and tail and the galaxy stellar rotation, we extract maps of the zeroth, first and second moment of the Hα ($\lambda 6563$) line and a map of the first mo-ment of the Ca II triplet ($\lambda\lambda\lambda 8498, 8542, 8662$), as detailed below. Throughout this analysis, for consistency with previous work (Sun et al. 2010; Jachym et al. 2014), we assume a systemic heliocentric velocity of $v_{sys} = 4661 \pm 46$ km s^{-1} for ESO137−001, equivalent to redshift $z_{sys} = 0.01555 \pm 0.00015$.

3.1 Emission lines

Maps of the Hα line flux $F_{H\alpha}$ (Figure 2), radial velocity relative to systemic $\Delta v = v - v_{sys}$ (Figure 5), and of the velocity dis-persion σ (Figure 6) are obtained from the final datacube using the IDL custom code KUBEVIZ. With KUBEVIZ, we fit a combina-tion of 1D Gaussian functions to the Hα and [NII] $\lambda\lambda 6548, 6583$ lines, keeping the relative velocity separation and the flux ratio of the two [NII] lines constant. While measuring the intrinsic line width σ, we also fix the instrumental line width σ_{ins} at each wave-length using an interpolation function constructed with a third de-gree polynomial fit to the resolution curve in the MUSE manual. At the observed wavelength of Hα computed for the systemic red-shift of ESO137−001 ($\lambda = 6664.87$ Å), we find $R = 2611.9$ or $\sigma_{ins} = 49$ km s^{-1}, in agreement with the resolution measured from skylines within a resampled datacube before sky subtraction. The spatial variation of the spectral resolution is found to be negligible for emission lines with an intrinsic width of $\gtrsim 10$ km s^{-1}.

Before the fit, the datacube is median filtered in the spatial direction with a kernel of 5×5 pixels to increase the individual
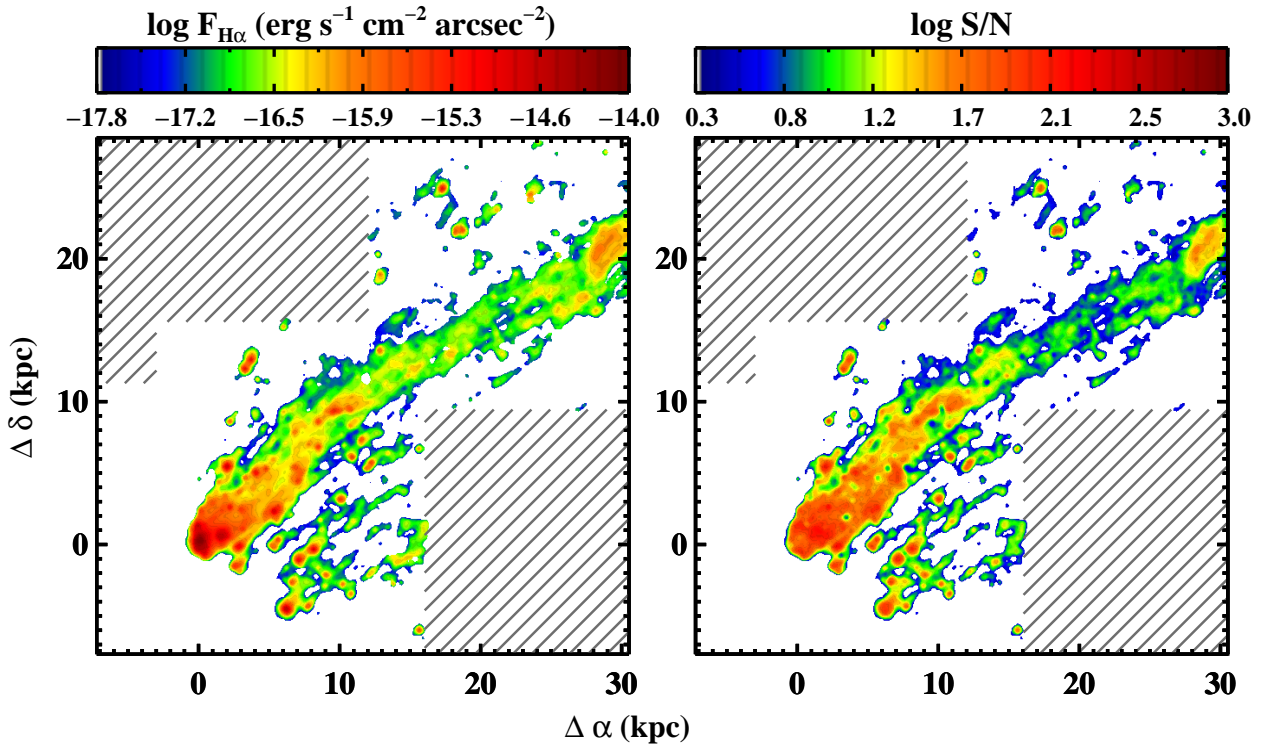
Figure 2. *Left:* Map of the Hα surface brightness at a resolution of 60×60 pc, obtained from the MUSE datacube as described in the text. Fluxes have been corrected for foreground Galactic extinction, but not for internal dust extinction. For visualization purposes, the map has been convolved with a median filter of 5×5 pixels. *Right:* The S/N map obtained by dividing the flux values by the associated errors in each pixel of the filtered datacube, which we have rescaled as described in the text. The dashed regions mark areas that are not covered by our observations. The image coordinate system is the same as the one adopted in Figure 1, but in proper physical units. The unprecedented depth of our MUSE observations uncover an extended primary tail, as well as a secondary southern tail with embedded HII regions.

S/N per pixel. No spectral smoothing is performed. In each spectrum, the continuum is then evaluated inside two symmetric windows around the Hα-[NII] line complex. Only values between the 40th and 60th percentile are modeled with a linear polynomial to estimate the continuum under each line. The Gaussian fit is performed on all the continuum-subtracted spaxels, assigning a minimum value of $\sigma = 1$ km s^{-1} to spectrally unresolved emission lines. During the fit, KUBEVIZ takes into account the noise from the "stat" datacube, thus optimally suppressing skyline residuals. However, the adopted variance underestimates the real error, most notably because it does not account for correlated noise. We therefore renormalize the final errors on the fitted parameters so as to obtain a reduced $\tilde{\chi}^2 \sim 1$. In the subsequent analysis, we mask spaxels where the S/N of the Hα flux is < 3 on the filtered data. Further masking is applied to the spaxels for which the line centroids or the line widths are extreme outliers compared to the median value of their distributions, or the errors on these quantities exceeds 50 km s^{-1} (i.e. conditions indicative of a non-converged fit). Throughout this analysis, the Hα flux has been corrected to account for appreciable Galactic extinction towards the Galactic plane ($A_{H\alpha} = 0.55$; Sun et al. 2007), but not for internal extinction. However, our conclusions primarily rely on kinematics and they are not affected by the presence of internal dust.

As a consistency check on the velocity measurements, we also model the [SII] $\lambda\lambda6717, 6731$ doublet following the same procedure. The derived velocities Δv from Hα and [SII] are found to be in excellent agreement, to better than 1 km s^{-1} on average over the entire cube. The difference in the two reconstructed velocity maps

is ~ 18 km s^{-1} for all regions where [SII] is detected at $S/N > 3$, and ~ 7 km s^{-1} where $S/N > 10$. A similar agreement is found when comparing the two measurements of velocity dispersion. In the following, we will only present and analyze the velocity field measured via Hα emission, the strongest transition, which we use as tracer for the bulk of the ionized hydrogen. A detailed analysis the properties of [SII] and other emission lines will be presented in the second paper of this series. We also note that, given the tracer used in our study, we will focus on the ram-pressure stripping of cold disk gas, which differ from the stripping of the hot gas in the halo or strangulation.

3.2 Absorption lines

Following a similar procedure to the one adopted for modeling emission lines, we extract the rotation curve of the stellar disk of ESO137−001 by fitting Gaussian functions to the Ca II triplet. Specifically, we apply to the datacube a median filter of 10×10 pixels in the spatial direction, with no filtering in the spectral direction. We then identify stars on the continuum-subtracted image in the rest-frame wavelength range $\lambda = 8380 - 8950$ Å, which we masks with circular regions of $1.2''$. The velocity relative to systemic is then found by fitting all the spaxels which have $S/N > 5$ per spaxels as measured on the filtered continuum image, using Gaussian functions with initial guesses at the rest-frame wavelengths of the Ca II triplet lines. We find that the best result is achieved by fitting only the strongest $\lambda8662$ line, a choice which reduces the noise introduced by poorly converged fits on the weaker transitions at the
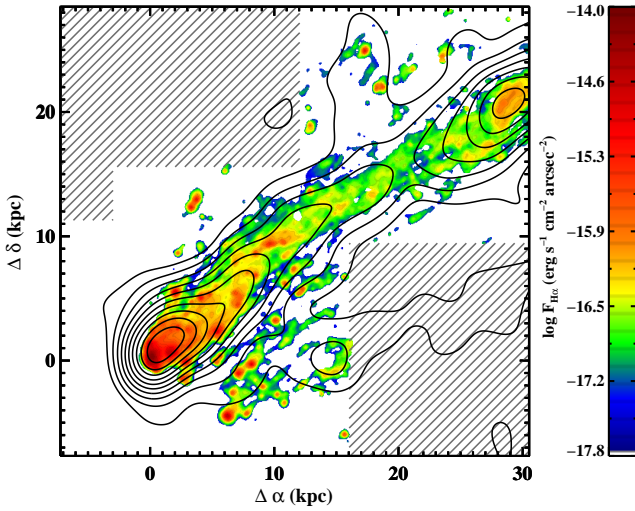
Figure 3. Same as the left panel of Figure 2, but with logarithmic contours from Chandra observations in steps of 0.05 dex to show the location of the X-ray emitting gas. The X-ray map has been smoothed, but in fact the X-ray front is at the same position of the Hα front (see Sun et al. 2010). While the primary X-ray and Hα tails are co-spatial, the Hα clumps identified by Sun et al. (2010) as HII regions do not correlate with the X-ray emission, as visible especially in the secondary southern tail.

Figure 4. Velocity map of the stellar component in the disk of ESO137−001 as traced by the Ca II triplet at a resolution of 60×60 pc. The map has been smoothed with a median filter of 10×10 pixels for visualization purposes. The dashed contours mark isophotes measured on the stellar continuum between $\lambda = 8380 - 8950$ Å, in steps of 0.4 mag arcsec^{-2}. The image coordinate system is the same as the one adopted in Figure 2, but within a smaller box centered at the galaxy position. The ordered velocity field is aligned with respect to the stellar isophotes implying that gravitational interactions cannot be the dominant mechanism for gas removal.

lowest S/N. A map of the reconstructed velocity field is in Figure 4.

The use of Gaussian functions, although rather simple, is preferred to full template fitting when handling ~ 10000 spaxels in order to reduce the run time of the analysis by orders of magnitude. Nevertheless, we have conducted extensive tests comparing results from Gaussian fits to results from full template fitting on a coarsely binned datacube, so as to verify that our method yields accurate centroids. For this test, we rebin the data using the Voronoi tessellation method with the code developed by Cappellari & Copin (2003). The binning procedure is performed on a continuum image in the rest-frame wavelength range $\lambda = 8380 - 8950$ Å, requiring a final S/N in the re-binned regions of > 80. Galactic stars are again identified and masked. We then fit to the optimally-combined spectra in each Voronoi cell templates from Cenarro et al. (2001), using the Penalized Pixel-Fitting method (pPXF) developed by Cappellari & Emsellem (2004). During the fitting procedure, we assume an instrumental line width at relevant wavelengths of $\sigma_{\rm ins} = 37$ km s^{-1}, computed as described in the previous section. Next, we apply our Gaussian fitting technique to the same binned spectra. When comparing these two independent measurements, we find a narrow Gaussian distribution, centered at 1.9 km s^{-1} and with standard deviation of 15 km s^{-1}, value which we assume as the typical uncertainty on the velocity measurement over the entire datacube. As for the case of emission lines, higher signal-to-noise regions are likely affected by smaller uncertainties. Furthermore, the 2D velocity field measured in the coarser Voronoi cells is in excellent agreement with the higher-resolution map recovered with Gaussian fits, confirming the robustness of the measurement presented in Figure 4.
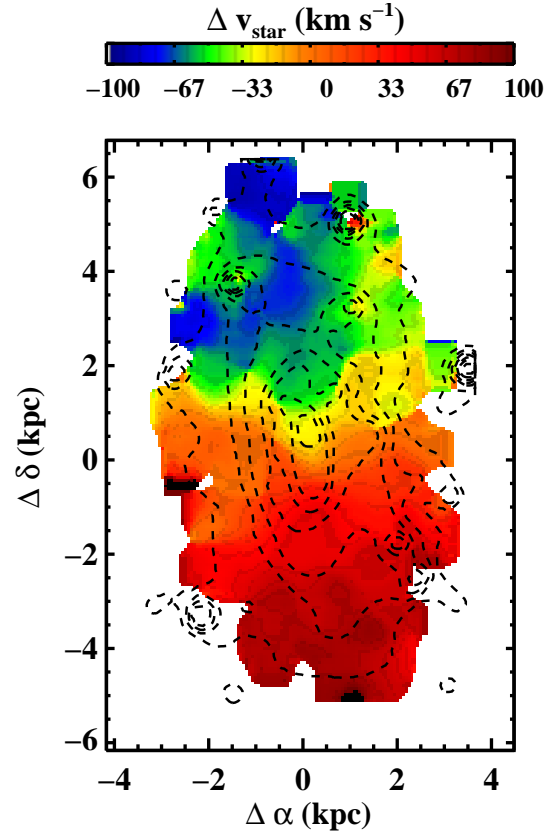
4 DISCUSSION

Compared to traditional narrow band imaging in $80 - 100$ Å wide filters, MUSE enables us to extract from the datacube flux maps in very narrow wavelength windows ($\sim 3 - 4$ Å), in which we optimally weight the signal from emission lines over the background sky noise. In addition, by fitting emission lines in each spatial pixel, we can more precisely recover the line flux also in the presence of bright unrelated sources, such as foreground stars, if the Poisson noise introduced by these sources does not outweigh the signal. These key advantages, combined with the large VLT aperture, allow us to reconstruct a map of the Hα emission in the disk and tail of ESO137−001 which is one order of magnitude deeper than previous observations (Sun et al. 2007), down to surface brightness limits of $F_{\rm H\alpha} \sim 10^{-18}$ erg s^{-1} cm^{-2} arcsec^{-2} (see Figure 2).

At this depth, our observations reveal that the Hα tail extends continuously for more than 30 kpc, with surface brightness between $F_{\rm H\alpha} \sim 10^{-17} - 10^{-16.5}$ erg s^{-1} cm^{-2} arcsec^{-2}. Figure 3 also shows that the Hα emission is co-spatial in projection with the primary X-ray tail. At the west edge of our field of view ($\Delta\alpha \sim 28$ kpc, $\Delta\delta \sim 21$ kpc), one can see a significant surface brightness enhancement, which is known to harbor $1.5 - 1.8 \times 10^{8} {\rm M}_{\odot}$ of molecular gas (Jachym et al. 2014) and it
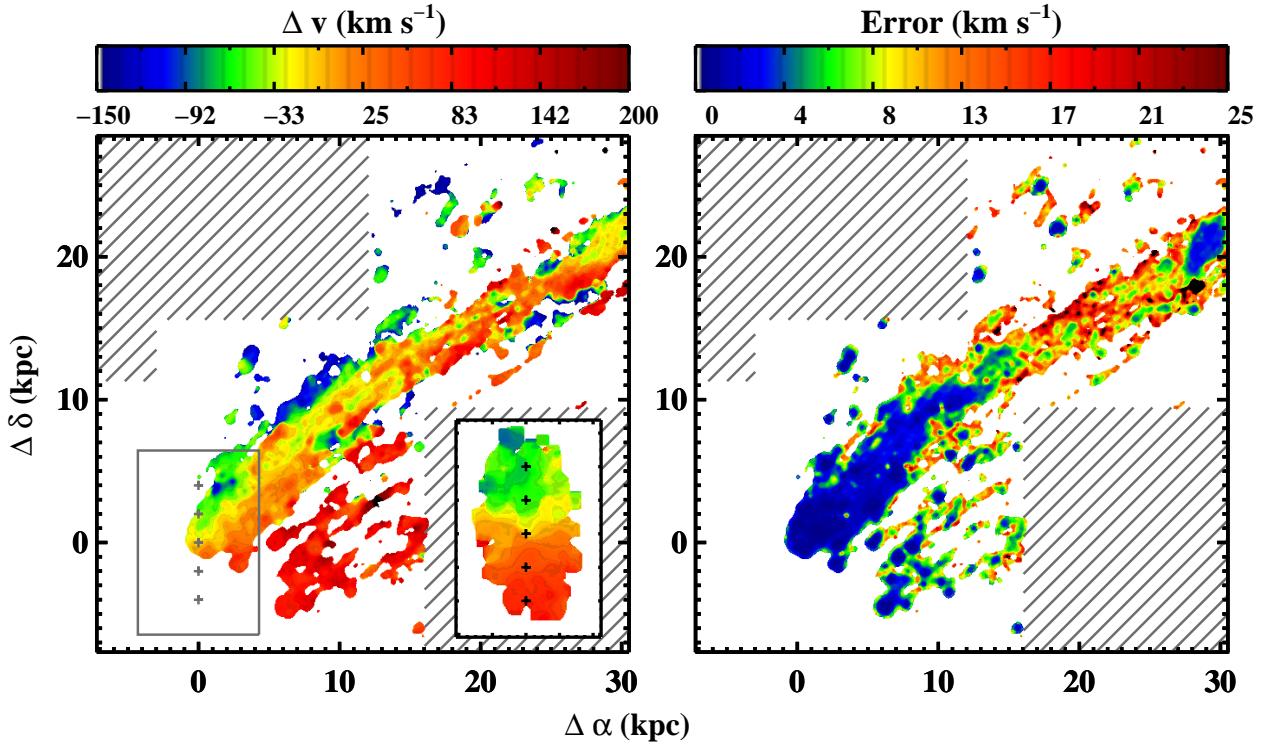
Figure 5. *Left:* Velocity map of the Hα line relative to the galaxy systemic redshift at a resolution of 60×60 pc, obtained from the MUSE datacube as described in the text. For visualization purposes, the map has been convolved with a median filter of 5×5 pixels. In the inset, we show the stellar kinematics from Figure 4, on the same color scale adopted for the gas velocity map. To facilitate the comparison, we show the position of the inset in the main panel (grey box), and we use crosses as a ruler with steps of 2 kpc. *Right:* The error map of the fitted centroids, rescaled as described in the text. The dashed regions mark areas which are not covered by our observations. The image coordinate system is the same as the one adopted in Figure 2. The gas and stellar kinematics are remarkably aligned to distances of ~ 20 kpc along the tail, suggesting that ESO137−001 is fast moving along a radial orbit in the plane of the sky.

is coincident with an X-ray bright region within the primary tail (Sun et al. 2010). On both sides of this primary tail, both towards north and south, we also detect a group of compact sources, some of which were previously identified as HII regions in long-slit spectroscopic observations by Sun et al. (2007) and Sun et al. (2010).

At the superior depth of our observations, the southern clump complex ($\Delta\alpha \sim 8$ kpc, $\Delta\delta \sim -2$ kpc) appears to be embedded in a lower surface brightness component, similar to the diffuse emission of the primary tail, stretching with the same projected orientation in the plane of the sky, with a position angle of approximately -54 deg. This second Hα tail is co-aligned with the secondary X-ray tail visible in the Chandra map, especially at the larger distances which are not probed by our observations, but which are visible in Sun et al. (2010) (their figure 2). Near the disk, the Hα emission in this secondary tail is dominated by bright Hα knots, which Sun et al. (2010) identified as HII regions. These HII regions are devoid of abundant hot plasma, and therefore the correlation between the X-ray flux and the secondary tail is not readily apparent, due to the limited spatial coverage of our observations that do not map the full extent of this southern tail.

Our observations, combined with the available HST imaging (see Figure 1), support a picture in which the galaxy ISM is being stripped at all galactocentric radii, from the outskirts to the inner core. Through models in which the efficiency of ram-pressure stripping depends on both gas density and galactocentric radius, as shown for example in figure 8 by Jachym et al. (2014), we can establish a correspondence between the spatial location of the Hα emitting gas and the time at which this gas was stripped. Moreover,

lower density material in the less-bound outskirts of ESO137−001 is stripped more easily at earlier times. This means that material originating from the disk outskirts traces a more rapid stripping process which will come to an end before the stripping from the nucleus. Our map shows that the Hα bright knots which are offset from the primary tail are being stripped from the northern and southern spiral arms, respectively. At these large galactocentric radii, there is no evidence of Hα emitting gas inside the stellar disk of ESO137−001 down to our sensitivity limit. Thus, ram-pressure has already cleared the galaxy ISM in these less-bound regions. Conversely, the galaxy ISM is still present in the inner $2 - 3$ kpc of ESO137−001 (see also Jachym et al. 2014), and this material is still being stripped, feeding the primary tail. We therefore conclude that the primary tail originates from the nucleus of ESO137−001 and not from the northern trailing arm, as suggested by the earlier analysis of Hα narrow-band imaging (Sun et al. 2010). This outside-in stripping process offers a natural explanation for the different morphology of the primary Hα tail compared to the two complexes of Hα bright clumps in the north and south direction. We speculate that the diffuse gas from the outer spiral arms was removed in the past and it has already mixed with the hot ambient medium downstream. As a consequence, we are now witnessing only the last episode of stripping of the densest clumps of gas, which trace the location of the older secondary tails. This is also a plausible explanation for why the primary Hα tail is narrow compared to the optical disk (Sun et al. 2010). Originally, there may have been a single tail, fed by material stripped at all galactocentric radii, differently than what we see today. A qualitative picture for how an
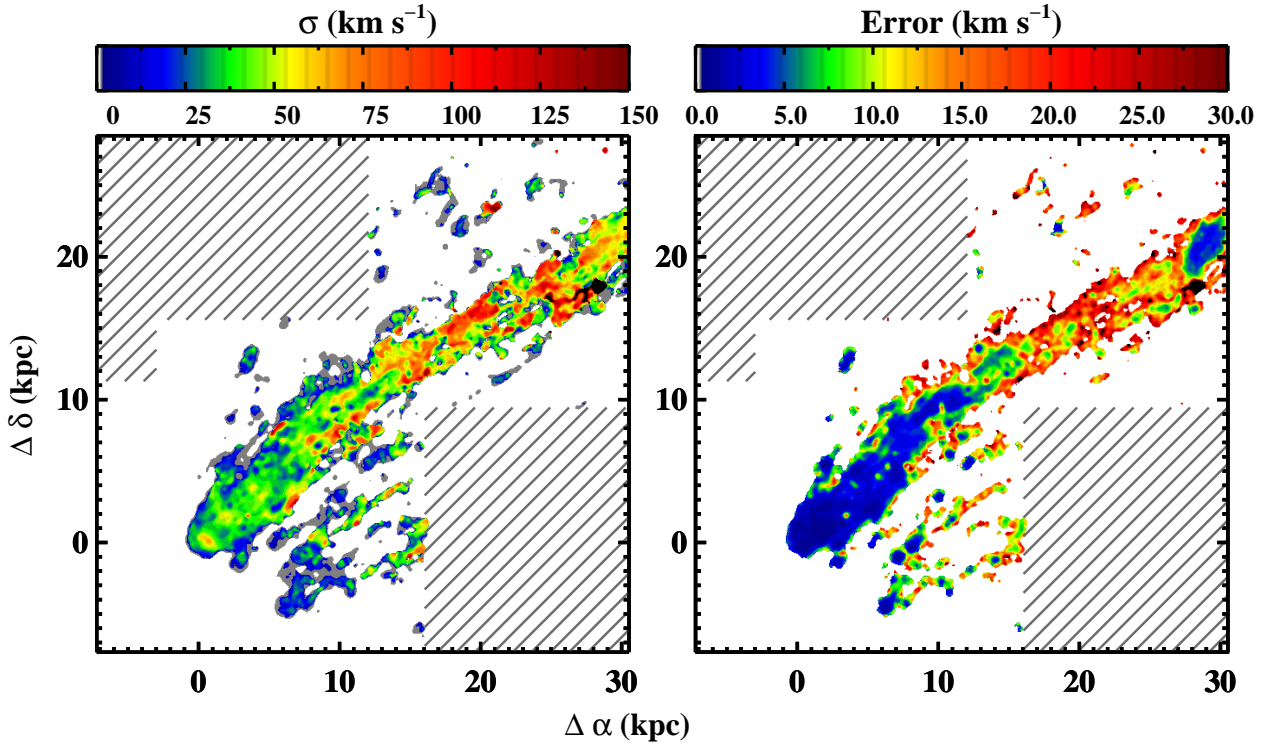
Figure 6. *Left:* Velocity dispersion map of the Hα line at a resolution of 60×60 pc, obtained from the MUSE datacube as described in the text. Values have been corrected for instrumental resolution, and pixels in which lines are unresolved are masked in grey. For visualization purposes, the map has been convolved with a median filter of 5×5 pixels. *Right:* The error map of the fitted line widths, rescaled as described in the text. The dashed regions mark areas which are not covered by our observations. The image coordinate system is the same as the one adopted in Figure 2. The transition from laminar to turbulent flow is seen at ~ 20 kpc from the galaxy center. For a model-dependent velocity of $\sim 3000 \, \mathrm{km \, s^{-1}}$, turbulence arises on timescales of $\sim 6.5 \mathrm{Myr}$.

inside-out stripping affects the morphology of the tail can be seen in the right panels of figure 1 in Quilis et al. (2000).

The analysis of the gas and stellar kinematics offers additional insight into how ram-pressure stripping occurs in ESO137−001 and how this galaxy moves as it approaches the center of the cluster. The Hα map shows that ESO137−001 is moving towards the center the Norma cluster on a projected orbit with position angle of $\sim -54 \deg$. The gas radial velocity, as traced by Hα (Figure 5), reveals no evident gradient along the primary tail, implying the motion occurs in the plane of the sky. Conversely, a clear velocity gradient is seen in the direction parallel to the galaxy major axis, perpendicular to the tail. This velocity pattern was already observed by Sun et al. (2010) who studied selected HII regions with Gemini/GMOS spectroscopy. The unprecedented quality of the MUSE datacube, however, drastically improves the fidelity with which the gas kinematics of ESO137−001 is traced, also within the diffuse component. Our observations confirm that ESO137−001 is approaching the cluster center on a nearly-radial orbit, with no significant tangential velocity component. The stripped gas retains a remarkable degree of coherence in velocity, which is originally imprinted by the rotation curve of the stellar disk. The map of the stellar kinematics (Figure 4) shows a clear rotational signature in the plane of the sky, with peak to peak velocity of $\pm 70 - 80 \, \mathrm{km \, s^{-1}}$ in projection out to radii of $4 - 5$ kpc. These values can be compared to the rotational velocity of $\sim 110 - 120 \, \mathrm{km \, s^{-1}}$, which Jachym et al. (2014) infer from the $K-$band luminosity. Radial velocities in excess to $\gtrsim 80 \, \mathrm{km \, s^{-1}}$ are visible in the stripped gas primarily in the southern secondary tail, which in our picture originates from material that detached from the spiral arm of ESO137−001 at radii

$\gtrsim 5$ kpc where stars rotate at comparable velocity (see inset in Figure 5). A hint of the same effect, but with reversed sign, is visible in the northern part of the primary tail where the stripped gas is blue-shifted compared to systemic velocity, in agreement with the velocity field of the stellar disk.

The infall velocity v_{inf} is unknown from direct observations, but we can combine several pieces of evidence to conclude that ESO137−001 is fast moving towards the center of the cluster. Given the cluster velocity dispersion, which Woudt et al. (2008) measured as $\sim 949 \, \mathrm{km \, s^{-1}}$ at 67 Mpc from the cluster center, one could estimate an orbital velocity $v_{\mathrm{los}} \sim 1600 \, \mathrm{km \, s^{-1}}$ for ESO137−001. However, the study of Jachym et al. (2014) suggests that a much higher velocity $\gtrsim 3000 \, \mathrm{km \, s^{-1}}$ is needed for an orbit that crosses the cluster virial radius. Furthermore, observations reveal that ESO137−001 suffers from extreme ram pressure which is able to ablate the gas even from the most bound regions of the galaxy potential. Such extreme ram pressure requires a high velocity encounter (Gunn & Gott 1972), and Jachym et al. (2014) estimates that during its interaction with the dense ICM, with electron densities of $1.0 - 1.4 \times 10^{-3} \, \mathrm{cm^{-3}}$ (Sun et al. 2010), ESO137−001 can suffer from ram pressure up to a peak of $\sim 2.1 \times 10^{-10} \, \mathrm{dyne \, cm^{-2}}$ for their assumed velocity.

As noted, a coherent radial velocity is visible on scales of at least $L_{\mathrm{coe}} \sim 20$ kpc from the galaxy center along the tail. Besides, the Hα emitting gas exhibits a modest degree of turbulent motion on similar scales, as seen from the velocity dispersion map (Figure 6). The bulk of the gas has a velocity dispersion $\sigma \sim 20 - 40 \, \mathrm{km \, s^{-1}}$, in qualitative agreement with the narrow CO line profiles shown by Jachym et al. (2014). A lower velocity dis-

persion ($\sigma \sim 15 - 25\,\mathrm{km\,s^{-1}}$) is seen in the bright Hα knots which are offset from the primary tail, as expected for a colder medium which hosts sites of ongoing star formation. Beyond $\sim 20\,\mathrm{kpc}$ from the galaxy position, a higher degree of velocity dispersion can be seen, with typical values above $\sim 40\,\mathrm{km\,s^{-1}}$ and peaks exceeding $\sim 100\,\mathrm{km\,s^{-1}}$. We need to be more cautious in interpreting kinematics within Field B, due to the lower signal to noise of our observations. Nevertheless, a progressively higher velocity dispersion moving far from the ESO137−001 disk along the tail was also noted by Jachym et al. (2014) who found larger FWHM and more complex line profiles in their CO observations at larger distances from the disk. Moreover, Gaussian fits to coarsely binned data with higher S/N show larger velocity widths in the outer tail, consistently with the measurements presented in Figure 6. Assuming an infall velocity $\gtrsim 3000\,\mathrm{km\,s^{-1}}$, gas lying at $\gtrsim 20\,\mathrm{kpc}$ from the ESO137−001 disk has been stripped $\sim 6.5\,\mathrm{Myr}$ ago, suggesting that substantial turbulence due to fluid instabilities or residual rotational velocity in the stripped gas grows on comparable timescales.

With simple arguments, we can relate this observed coherence to the fact that the infall velocity $v_{\rm inf}$ greatly exceeds the galaxy circular velocity $v_{\rm cir}$. Absent a restoring centripetal force, material ablated from the disk at a radius $r_{\rm det}$ with circular velocity $v_{\rm cir} = v_{\rm los}/\sin i$ (where $i = 66\,\mathrm{deg}$ is the disk inclination angle and $v_{\rm los}$ is the observed line of sight velocity) would leave on a tangential orbit, causing the tail to flare. Unsurprisingly, this is not what we observe, given that the diffuse gas in the tail is likely to be confined, e.g., by the ambient ICM pressure. However, a laminar flow on scales $L_{\rm coe}$ implies only a modest shear between the ambient ICM and the Hα emitting gas, and thus the tail cannot be fast spinning as ESO137−001 travels for $L_{\rm coe}$. In a simple geometry, a parcel of gas in the tail rotates by an angle $\alpha_{\rm rot} \approx \frac{L_{\rm coe}}{r_{\rm det}} \times \frac{v_{\rm cir}}{v_{\rm inf}}$, and thus the lack of substantial turbulence leads us to conclude that $v_{\rm cir} \ll v_{\rm inf}$. Detailed comparisons of the Hα surface brightness and velocity maps with the results of new hydrodynamic simulations that reproduce the properties of ESO137−001 are now wished for to characterize quantitatively the interaction of the warm/hot components, the effect of hydrodynamic and thermal instabilities, and the role of magnetic fields, which are all encoded in the phenomenology revealed by our MUSE observations.

To conclude our analysis on the kinematic properties of ESO137−001 and its tail, we note how the stellar velocity field in Figure 4 exhibits an ordered velocity gradient along the major axis, as expected for a nearly edge-on rotating disk. Compared to the isophotes measured on an image extracted from the datacube in the wavelength range $\lambda = 8380 - 8950\,\text{Å}$, the measured velocity field appears to be symmetric relative to the major axis and it is also well-centered at the optical location of ESO137−001. This ordered motion and an extremely distributed morphology of the ISM compared to unperturbed isophotes point to ram-pressure stripping as the leading mechanism responsible for the gas ablation. In fact, ram-pressure stripping produces only subtle transformations in the stellar disks (e.g. Smith et al. 2012b), which largely retain memory of the original morphology and kinematics (e.g. Boselli et al. 2008; Toloba et al. 2011). Moderate perturbations in the velocity field, visible especially in the northern part of the stellar disk, or in the shapes of the isophotes, such as a small bend in the southern portion of the disk, are not surprising given the small projected separation ($\sim 267\,\mathrm{kpc}$) of ESO137−001 with respect to the bright cluster galaxy. Gravitational interactions from an early stage of merger with the dark matter halo of this central massive galaxy are likely present, but nevertheless they do not appear to be the main mechanism for gas removal.

5   SUMMARY AND FUTURE WORK

In this paper we have presented MUSE science verification observations of the central disk and gaseous tail of ESO137−001, a spiral galaxy infalling at high velocity on a nearly-radial orbit towards the center of the massive Norma cluster at $z \sim 0.0162$. During its encounter with the ICM, ESO137−001 is experiencing extreme ram-pressure stripping which gives rise to an extended tail which has been detected at multiple wavelengths, from the X-ray to the radio. The capabilities of MUSE, with its large field of view, extended wavelength coverage, and high throughput, have allowed us to map the Hα emitting gas inside ESO137−001 and its tail to surface brightness limits of $F_{\rm H\alpha} \sim 10^{-18}\,\mathrm{erg\,s^{-1}\,cm^{-2}\,arcsec^{-2}}$, and to reconstruct the stellar kinematics traced by the Ca II triplet.

These new data offer an unprecedented view of ESO137−001 and its tail, which is traced in Hα emission to beyond 30 kpc. These observations allow us to conclude that the ISM of this galaxy is being stripped at all galactocentric radii: the less bound material has been completely stripped from the spiral arms, giving rise to clumpy and irregular tails, while the galaxy center still contains part of the original ISM which feeds the primary Hα tail, aligned with the X-ray emission. The stripped gas retains the original rotation velocity of the stellar disk, but exhibits a remarkable degree of coherence in velocity space for $\sim 20\,\mathrm{kpc}$ downstream. Beyond $\sim 20\,\mathrm{kpc}$ from the galaxy disk along the tail, a greater degree of turbulence is seen, with peak velocity dispersion $\gtrsim 100\,\mathrm{km\,s^{-1}}$. These pieces of evidence are indicative that the galaxy is fast moving in the plane of sky, with infall velocity much greater than the rotational velocity. For an infall velocity of $\sim 3000\,\mathrm{km\,s^{-1}}$, indicated by the orbital study of Jachym et al. (2014), material at $\sim 20\,\mathrm{kpc}$ has been stripped approximately $\sim 6.5\,\mathrm{Myr}$ ago, suggesting that the transition from laminar to turbulent flow occurs on similar timescales. Finally, the ordered stellar rotation combined with regular isophotes in the disk rules out gravitational interactions as the main process responsible for the stripping, although some disturbances are present given that ESO137−001 has started to merge with the dark matter halo of the bright central cluster galaxy.

This work offers only a first glimpse of the rich MUSE datacube, in which we detect multiple transitions including [OIII], [OI], [NII], [SII], Hβ in emission, as well as absorption lines within the stellar disk, most notably Ca II and Hα. All these transitions will allow us to better constrain the physical properties of the disk and tail of ESO137−001, including the properties of the bow shock and the interaction between the stripped warm ISM and the hot X-ray emitting plasma. Furthermore, a detailed comparison of these observations with results of numerical simulations will be crucial to establish the hydrodynamic and thermal properties of the gas which is subject to ram-pressure stripping, including the role of instabilities and magnetic fields. These studies will be presented in future papers of this series.

Our work demonstrates the terrific potential that MUSE and future large field-of-view IFUs on 8-10m class telescopes have in studying ram-pressure stripping. By targeting galaxies like ESO137−001 in which ram pressure is near to its maximum, these observations will provide key information on how gas is ablated from all galactocentric radii, how the diffuse and dense ISM components interact and mix with the ambient ICM, and on what timescales star formation responds to this gas removal. Once applied to more typical cluster galaxies, results from these detailed analyses will offer a comprehensive view of how ram pressure affects the build-up of the observed red sequence in rich clusters. In turn, this will help to disentangle the role of environment from the

role of internal processes in shaping the color bimodality seen in the densest regions of the universe.

REFERENCES

Arrigoni Battaia, F., Gavazzi, G., Fumagalli, M., et al. 2012, A&A, 543, A112

Bacon, R., Accardo, M., Adjali, L., et al. 2010, Proc. SPIE, 7735, 9

Baldry, I. K., Glazebrook, K., Brinkmann, J., et al. 2004, ApJ, 600, 681

Balogh, M., Eke, V., Miller, C., et al. 2004, MNRAS, 348, 1355

Bekki, K., & Couch, W. J. 2003, ApJ, 596, L13

Bell, E. F., Wolf, C., Meisenheimer, K., et al. 2004, ApJ, 608, 752

Boselli, A., & Gavazzi, G. 2006, PASP, 118, 517

Boselli, A., Boissier, S., Cortese, L., & Gavazzi, G. 2008, ApJ, 674, 742

Bower, R. G., Lucey, J. R., & Ellis, R. S. 1992, MNRAS, 254, 601

Brammer, G. B., Whitaker, K. E., van Dokkum, P. G., et al. 2009, ApJ, 706, L173

Cappellari, M., & Emsellem, E. 2004, PASP, 116, 138

Cappellari, M., & Copin, Y. 2003, MNRAS, 342, 345

Cenarro, A. J., Cardiel, N., Gorgas, J., et al. 2001, MNRAS, 326, 959

Cortese, L., Gavazzi, G., Boselli, A., et al. 2006, A&A, 453, 847

Dressler, A., Oemler, A., Jr., Poggianti, B. M., et al. 2013, ApJ, 770, 62

Ebeling, H., Stephenson, L. N., & Edge, A. C. 2014, ApJ, 781, L40

Fossati, M., Gavazzi, G., Boselli, A., & Fumagalli, M. 2012, A&A, 544, A128

Fumagalli, M., & Gavazzi, G. 2008, A&A, 490, 571

Fumagalli, M., Gavazzi, G., Scaramella, R., & Franzetti, P. 2011, A&A, 528, A46

Gavazzi, G., Fumagalli, M., Cucciati, O., & Boselli, A. 2010, A&A, 517, A73

Gavazzi, G., Bonfanti, C., Sanvito, G., Boselli, A., & Scodeggio, M. 2002, ApJ, 576, 135

Gavazzi, G., Boselli, A., Mayer, L., et al. 2001, ApJ, 563, L23

Gavazzi, G., & Jaffe, W. 1985, ApJ, 294, L89

Gunn, J. E., & Gott, J. R., III 1972, ApJ, 176, 1

Hashimoto, Y., Oemler, A., Jr., Lin, H., & Tucker, D. L. 1998, ApJ, 499, 589

Henden, A. A., Levine, S. E., Terrell, D., Smith, T. C., & Welch, D. 2012, Journal of the American Association of Variable Star Observers (JAAVSO), 40, 430

Hester, J. A., Seibert, M., Neill, J. D., et al. 2010, ApJ, 716, L14

Hinshaw, G., Larson, D., Komatsu, E., et al. 2013, ApJS, 208, 19

Jachym, P., Combes, F., Cortese, L., Sun, M., & Kenney, J. D. P. 2014, arXiv:1403.2328

Kauffmann, G., White, S. D. M., Heckman, T. M., et al. 2004, MNRAS, 353, 713

Kenney, J. D. P., Geha, M., Jáchym, P., et al. 2014, ApJ, 780, 119

Kenney, J. D. P., Tal, T., Crowl, H. H., Feldmeier, J., & Jacoby, G. H. 2008, ApJ, 687, L69

Kronberger, T., Kapferer, W., Ferrari, C., Unterguggenberger, S., & Schindler, S. 2008, A&A, 481, 337

Larson, R. B., Tinsley, B. M., & Caldwell, C. N. 1980, ApJ, 237, 692

Lewis, I., Balogh, M., De Propris, R., et al. 2002, MNRAS, 334, 673

Nishino, S., Fukazawa, Y., & Hayashi, K. 2012, PASJ, 64, 16

Nulsen, P. E. J. 1982, MNRAS, 198, 1007

Moore, B., Katz, N., Lake, G., Dressler, A., & Oemler, A. 1996, Nature, 379, 613

Quilis, V., Moore, B., & Bower, R. 2000, Science, 288, 1617

Roediger, E., Brüggen, M., Owers, M. S., Ebeling, H., & Sun, M. 2014, arXiv:1405.1033

Ruszkowski, M., Brüggen, M., Lee, D., & Shin, M.-S. 2014, ApJ, 784, 75

Sivanandam, S., Rieke, M. J., & Rieke, G. H. 2010, ApJ, 717, 147

Smith, R. J., Lucey, J. R., Price, J., Hudson, M. J., & Phillipps, S. 2012, MNRAS, 419, 3167

Smith, R., Fellhauer, M., & Assmann, P. 2012, MNRAS, 420, 1990

Strateva, I., Ivezić, Ž., Knapp, G. R., et al. 2001, AJ, 122, 1861

Sun, M., Donahue, M., Roediger, E., et al. 2010, ApJ, 708, 946

Sun, M., Jones, C., Forman, W., et al. 2006, ApJ, 637, L81

Sun, M., Donahue, M., & Voit, G. M. 2007, ApJ, 671, 190

Toloba, E., Boselli, A., Cenarro, A. J., et al. 2011, A&A, 526, A114

Tonnesen, S., & Bryan, G. L. 2010, ApJ, 709, 1203

Vollmer, B., Cayatte, V., Balkowski, C., & Duschl, W. J. 2001, ApJ, 561, 708

Vollmer, B., Balkowski, C., Cayatte, V., van Driel, W., & Huchtmeier, W. 2004, A&A, 419, 35

Weiner, B. J., Phillips, A. C., Faber, S. M., et al. 2005, ApJ, 620, 595

Woudt, P. A., Kraan-Korteweg, R. C., Lucey, J., Fairall, A. P., & Moore, S. A. W. 2008, MNRAS, 383, 445

Yagi, M., Yoshida, M., Komiyama, Y., et al. 2010, AJ, 140, 1814

Yoshida, M., Yagi, M., Okamura, S., et al. 2002, ApJ, 567, 118